INSTITUTE OF PHYSICS PUBLISHING PHYSICS IN MEDICINE AND BIOLOGY

Phys. Med. Biol. **50** (2005) 5557–5572 doi:10.1088/0031-9155/50/23/010

Spectral image reconstruction for transcranial ultrasound measurement

Greg T Clement

Department of Radiology, Harvard Medical School, Brigham and Women's Hospital, Boston, MA 02115, USA

Received 21 June 2005, in final form 21 September 2005
Published 16 November 2005
Online at stacks.iop.org/PMB/50/5557

Abstract

An approach aimed at improved ultrasound resolution and signal strength through highly attenuating media is presented. The method delivers a series of multiple-cycle bursts in order to construct a discrete spectral (frequency domain) response in one dimension. Cross-correlation of this ultrasound A-mode response with its transmitted signal results in time-localized peaks that correspond to scattering locations. The approach is particularly relevant to the problem of transcranial ultrasound imaging, as it combines numerous smaller signals into a single signal whose net power may exceed that which could be achieved using a single burst. Tests are performed with human skull fragments and nylon-wire targets embedded in a tissue phantom. Skulls are oriented to produce both lateral and shear modes of transcranial propagation. A total of nine locations distributed over three *ex vivo* human skull samples are studied. Compared with pulsed and chirped signals, results indicate more localized peaks when using the multi-cycle approach, with more accurate positioning when combined with the transcranial shear mode.

(Some figures in this article are in colour only in the electronic version)

1. Introduction

Although it has long been recognized that transcranial ultrasound holds the potential for detecting an extensive range of brain disorders (Wall *et al* 1953, Barrows *et al* 1964, Grossman 1964, Fry 1968, Erikson *et al* 1974, Smith *et al* 1978, 1979), strong attenuation and distortion by the skull bone has limited its practical clinical use to Doppler imaging through the temporal bone window (Berg and Becker 2002) for injury detection (Shigemori *et al* 1990) and tumour detection (Becker *et al* 1994). However, methods such as tomographic reconstructions have been explored (Dines *et al* 1981, Koivukangas *et al* 1986, Britt *et al* 1987), and recent feasibility studies have examined improved imaging techniques such as perfusion imaging (Wiesmann and Seidel 2000, Seidel *et al* 2000, Harrer *et al* 2003) and real-time 3D imaging (Smith *et al* 2004) for volumetric time histories in the brain. There has also been an effort

0031-9155/05/235557+16$30.00

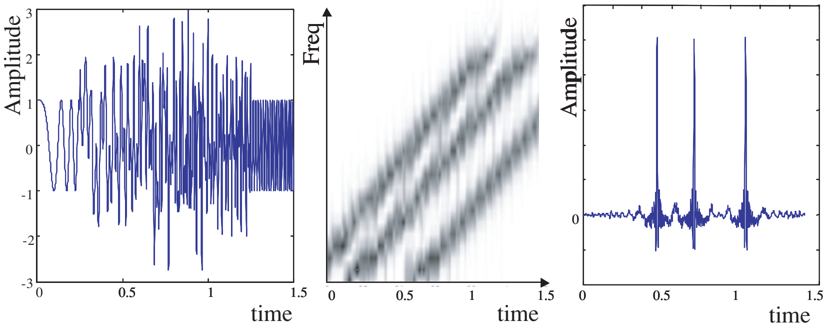

Figure 1. (Left) Received signal from three reflections using a chirp. (Centre) Spectrogram of the signal separating the three objects. (Right) The same signal after cross-correlation of the received and transmitted signals.

to propagate ultrasound through a larger region of bone, including thicker and more complex regions (Baikov *et al* 2003a, 2003b), in order to expand the quality and volume of the brain volume to be imaged.

A recent and now widely studied approach towards increasing ultrasound signal strength is the application of coded excitations (O'Donnell and Flax 1988, Shen and Ebbini 1996, Misaridis *et al* 2000), which have been suggested for numerous applications, including brain imaging (Montaldo *et al* 2005). Chirp-encoded excitation, in particular, is suitable for constructing time-localized signals through regions containing high attenuation due to its spectral similarity to a broadband pulse (Pedersen *et al* 2003). This method calculates the cross-correlation between the transmitted and received chirp signals, producing localized pulses in time corresponding to scattering locations. The physical origin of this localization may be elucidated with a time–frequency analysis (spectrogram) of an idealized received chirp signal caused by reflections from three objects (figure 1). The spectrogram clearly shows separation of individual objects. After correlation with the transmitted chirp, three distinct peaks are visible in the time domain, corresponding to the echoes cased by the reflecting objects.

It is interesting, however, that the cross-correlation of a summation of continuous-wave (nonlocalized) signals also contains localized signal information. The present study demonstrates this procedure and uses it to measure reflections through human skull fragments. In the experiment, a series of individual extended (multi-cycle) bursts are sent through skull bone, and the amplitude and phase of the return signal are recorded. The bursts are repeated over a range of frequencies and then numerically combined to construct a frequency spectrum. As described below, after a matched filter is applied, sharp temporal peaks are expected corresponding to reflection points in the data.

There are several expected advantages of the proposed technique over pulsed and chirped signals. First, the use of multi-cycle bursts will allow the transducer to send relatively strong signals at each component in the spectrum. Second, the input power can be increased for the higher, more attenuating frequencies. Having a normalized spectrum across the frequency domain should allow better localization of interfaces after matched filtering is applied. Third, forced driven oscillations of the transducer are expected to somewhat increase the transducer's bandwidth at the high and low ends of its response. In this case, higher driving amplitudes are applied to regions away from mechanical resonance. Fourth, the combined signal will have a net power far exceeding powers that could safely be achieved with a single burst. That is, the net signal will be composed of the summation of each multi-cycle signal.

In addition to attenuation, the ranges of transcranial procedures investigated are all subject to reflections and diffractions caused by irregularities in the skull's shape, density and sound speed. These properties collectively contribute towards distorting an ultrasound beam, which could be phase corrected given sufficient information about the skull and a sufficient number of array elements (Clement and Hynynen 2002, Aubry *et al* 2003). However, in recent work (Clement *et al* 2004), it was observed that under certain conditions it is possible to propagate ultrasound through the skull with reduced distortion by using high incident angles. Both numeric and experimental investigations suggest that this is due to the behaviour of shear modes induced in the skull bone. When the ultrasound angle of entry is beyond Snell's critical angle for the longitudinal pressure wave, propagation in the bone is primarily due to a shear wave. However, similarities between the sound speed in soft tissue and the shear wave speed of bone indicate that this conversion from a longitudinal wave to a shear wave, and then back to a longitudinal wave in the brain does not necessarily produce a highly distorted signal. Our investigations, which studied isotropic phantom materials and later *ex vivo* human bone samples, support this hypothesis (Clement *et al* 2004).

High attenuation, however, remains an obstacle in both the longitudinal and shear propagation modes, particularly at frequencies above 1 MHz where the absorption coefficient grows rapidly with frequency (Fry and Barger 1978, White 2005). It is anticipated that the coded excitation scheme will offset this attenuation by increasing the overall signal. Used in the shear mode, any undesired effects of standing waves and strong reflections from bone interfaces will be diminished by angling deflecting reflected ultrasound away from the receiver. To test the method, we perform a series of A-line images through nine locations using three *ex vivo* human calvarias. Experiments are performed in both longitudinal and shear modes. To evaluate the multi-cycle coding scheme, the measurements are compared with a broadband (pulsed) signal as well as with the linear frequency modulated chirp (Pedersen *et al* 2003).

2. Theory

In ultrasound, signals with broadband content are generally desirable in order to produce time-localized signals, providing higher resolution in the ultrasound's direction of propagation. However, equivalent bandwidth may be produced with a chirped signal, but with frequencies spread out over a specified period of time. In this case, signals from reflected objects tend to be rather complicated, since signals from two or more reflections will be superimposed over an extended time period (figure 1, left). Chirp-coded excitation techniques apply a matched filter, which correlates the initial outgoing signal with the received signal. The result is a time-localized peak at the point of reflections (figure 1, right).

The multi-cycle scheme similarly is designed to construct a broadband signal. However, it performs this operation in a series of nearly harmonic bursts and assembles the received signal directly in the frequency domain. The primary expected advantage of the combined multi-cycle scheme is a significant increase in the overall signal strength. Secondary advantages include the ability to normalize the signal referenced to its impulse response in the frequency domain, creating an even response, and the ability to drive the transducer somewhat beyond its bandwidth. The case is illustrated for a planar signal operated in a CW mode,

$$\tilde{p}_{\mathrm{r}\omega}(t) = p_{\mathrm{r}}(\omega)\sin(\omega t + \phi_{\mathrm{r}}(\omega)), \tag{1}$$

where p_{r} and ϕ_{r} are the amplitude and phase relative to the source driving potential at angular frequency ω. The subscript r denotes a reference signal, indicating the signal in free space. As illustrated in figure 2(a), if this signal encounters first a region with variable sound speed followed by a region of interest (ROI) containing a series of backscattering sources at locations

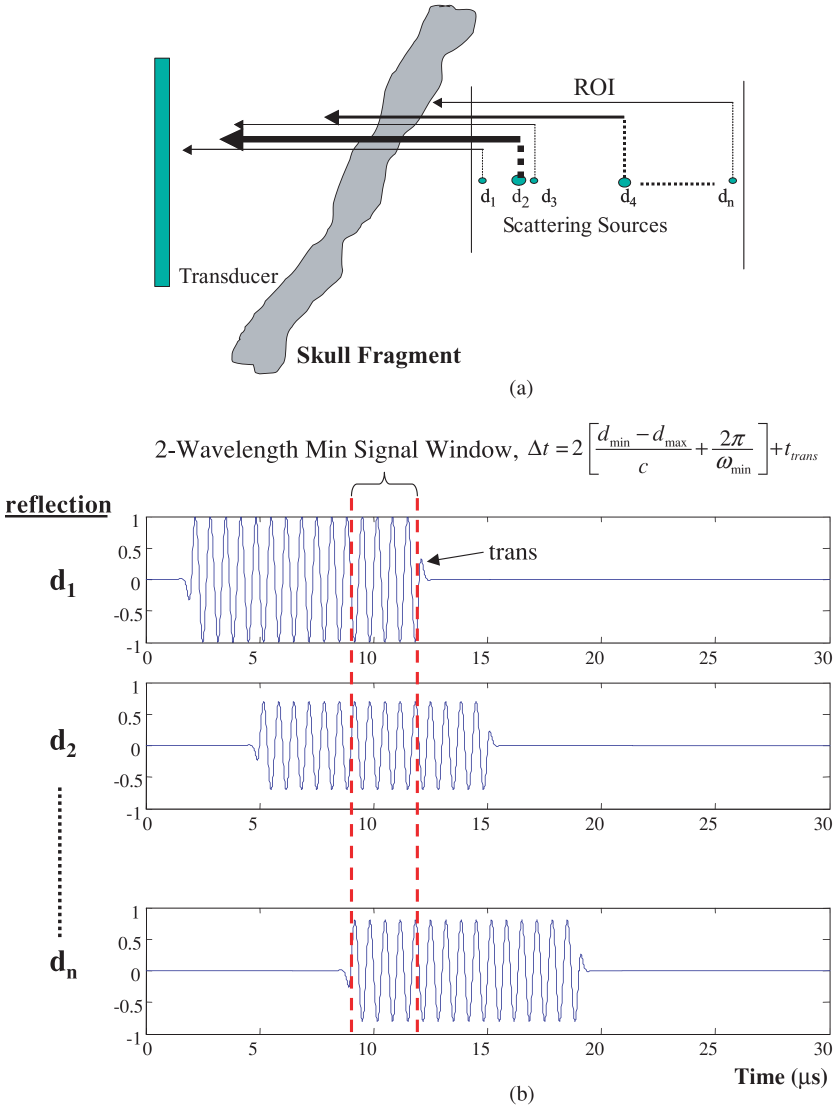

Figure 2. (a) Conceptual diagram of the contributions to the received signal; a sinusoid whose amplitude and phase are determined by the location and strength of scatterers d_n. (b) The time position of the signal record window as determined by the front $d_{\min}$ and rear $d_{\max}$ of the ROI.

d_n within an otherwise homogeneous region of sound speed c, the received signal at the source will be

$$\tilde{p}_\omega(-t) = \sum_{n=1}^{N} p_n(\omega) \sin\left(\omega t + \frac{2\omega d_n}{c} + a\omega + \phi_{\mathrm{r}}(\omega)\right), \tag{2}$$

where $a\omega$ represents a cumulative phase shift caused by propagation between the source and the ROI, and p_n is the source strength of each backscattered wave. The received signal is simply a harmonic wave whose amplitude and relative phase are determined by the linear superposition of the scattered signals. The task of identifying the locations d_n is achieved by acquiring $\tilde{p}_{\mathrm{r}\omega}$ over a range of frequencies ($\omega_{\min}$, $\omega_{\max}$), so that a discrete sampling of the signal in the frequency domain may be assembled.

The discrete, normalized frequency space for the reference signal may be expressed as

$$\tilde{P}_{\mathrm{r}}(\omega) = \begin{cases} \mathrm{e}^{\mathrm{i}\phi_{\mathrm{r}}(\omega)}, & \omega_{\min} \leqslant \omega \leqslant \omega_{\max}, \\ 0, & \text{otherwise.} \end{cases} \tag{3}$$

Similarly, a reflected signal after undergoing an arbitrary number of reflections is expressed as

$$\tilde{P}(\omega) = \begin{cases} \dfrac{p(\omega)}{p_{\mathrm{r}}(\omega)}\, \mathrm{e}^{\mathrm{i}(\phi_{\mathrm{s}}(\omega)+a\omega)}, & \omega_{\min} \leqslant \omega \leqslant \omega_{\max}, \\ 0, & \text{otherwise,} \end{cases} \tag{4}$$

where the reflected signal amplitude is normalized by the reference amplitude. Recovery of reflection points in time is based on the fact that (1) the auto-correlation of any wide-band signal with a signal proportional to itself produces a time-localized signal, regardless of whether the signal itself is time localized, and (2) the auto-correlation theorem,

$$q(t) = \int_{-\infty}^{\infty} \tilde{p}_{\mathrm{r}}(t')\tilde{p}(t+t')\,\mathrm{d}t' = \mathrm{IFT}\{\tilde{P}_{\mathrm{r}} * (\omega)\tilde{P}(\omega)\}, \tag{5}$$

implies that the reflected signals will be time localized. The return signal is understood to be time-inverted and the asterisk connotes a complex conjugate. Given a sufficiently wide range of measurement frequencies and an appropriate sampling rate, $q(t)$ will consist of time-localized peaks from each reflection. Unlike chirp-encoded excitation, the approach discretely assembles the signal in the frequency domain. This signal does not require phase control of the output signals, since the product given in brackets in equation (5) is independent of output phase. Similarly, the filtered signal is independent of ϕ_{r}, the source's phase relative to the transducer driving potential.

To minimize interference away from the ROI, the continuous-wave signals described above are replaced by short multi-cycle bursts. The bursts must be long enough to allow a region of signal mixing between the steady-state (non-transient) signals of each backscattered interface. Thus, given a measurement area within the ROI between axial distances $d_{\min}$ and $d_{\max}$, the burst length must be extended over a period

$$\Delta t = 2\left[\frac{d_{\min} - d_{\max}}{c} + \frac{2\pi}{\omega_{\min}}\right] + t_{\mathrm{trans}}, \tag{6}$$

where t_{trans} represents the transient time and signals are measured in a signal window spanning the length of two cycles of the minimum frequency, as shown in figure 2(b). By the Nyquist sampling theorem, the length of the ROI determines the resolution necessary to construct the frequency space, which must have frequency steps of at least $c/2(d_{\max} - d_{\min})$ to avoid undersampling.

3. Experimental methods

The experiment was designed to test the approach in the presence of a strong scatterer and attenuator between the source and the ROI. Formaldehyde-fixed human skull fragments were used for this purpose. For each fragment, four different measurement scenarios were considered: (i) a multi-cycle excitation recorded over the −6 dB bandwidth using a *fixed driving potential* at each frequency, (ii) a multi-cycle excitation over the −12 dB bandwidth using a variable driving potential set to provide *fixed acoustic output* at each frequency, (iii) a chirped output, and (iv) a broadband pulse. Each of these measurements was performed in a water bath with a human skull placed between a broadband focused transducer and a

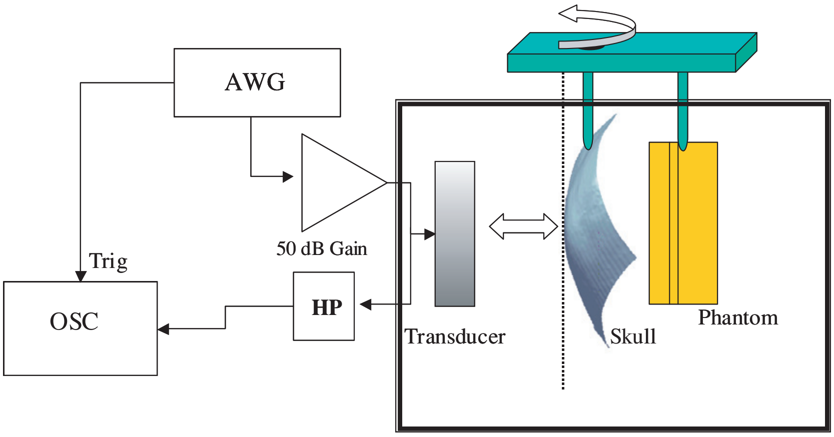

Figure 3. The experimental setup. An arbitrary waveform generator (AWG) sends signals through an rf amplifier and to a broadband transducer. The received signal is sent through a high-pass filter (HP) before being recorded by an oscilloscope (OSC).

tissue phantom, as illustrated in figure 3. First the skull was positioned so that its surface was approximately parallel to the oncoming wavefront. All measurements were then repeated with the skull fragment oriented at angles $>35^\circ$ relative to the propagation axis, which is generally beyond Snell's critical angle for the longitudinal mode at a skull–water interface. In this case, waves were converted from longitudinal in water to shear in the bone and then back into longitudinal when exiting the skull. This conversion sequence was repeated for the backscattered signal.

All measurements were performed in a tank filled with deionized water. The transducer (Imasonics, Lyon, France, radius of curvature = 120 mm, resonant frequency = 1.1 MHz) was composed of 64 electrically coupled elements, which acted as a single element with a diameter of approximately 45 mm. A single element at the centre of the array was used as a receiver. The skull fragments were placed approximately 130 mm from the transducer surface and the ROI, located between 145 and 215 mm from the transducer and coinciding with the focal region of the transducer. Care was taken to assure that the entire beam was propagated through the skull *en route* to the ROI. When shear waves were used as the mode of transskull propagation, the angle of the skull relative to the incident beam was determined by measuring the angle between the transducer's axis of symmetry and the peak of the signal reflected from the skull surface, the angle of incidence being half this value. A phantom consisting of nylon wires embedded in a tissue-mimicking matrix (Madsen *et al* 1998) was placed within the ROI. Scattering interfaces consisted of the water/phantom interface ($d_1 = 150$ mm), a 0.5 mm diameter wire ($d_2 = 170$ mm), another 0.5 mm diameter wire ($d_3 = 180$ mm) and the phantom/water interface ($d_4 = 200$ mm).

The transducer input signal was generated by an arbitrary waveform generator (Wavetek model 395, Fluke Precision Measurement, San Diego, CA) and amplified by a power amplifier (ENI, model 3100L, Rochester, NY). Received signals were sent through a high-pass filter set at 1 kHz to eliminate dc drift (Preamble Instruments, Beaverton, OR) before being recorded by a digital oscilloscope (Textronix, model 380, Beaverton, OR), and downloaded to a PC. Frequency, pulse duration and amplitude on the waveform generator as well as oscilloscope settings and waveform retrieval were all software-controlled through a GPIB interface. For the multi-cycle signals, a 5 μs data string was recorded for each frequency step 289 μs after

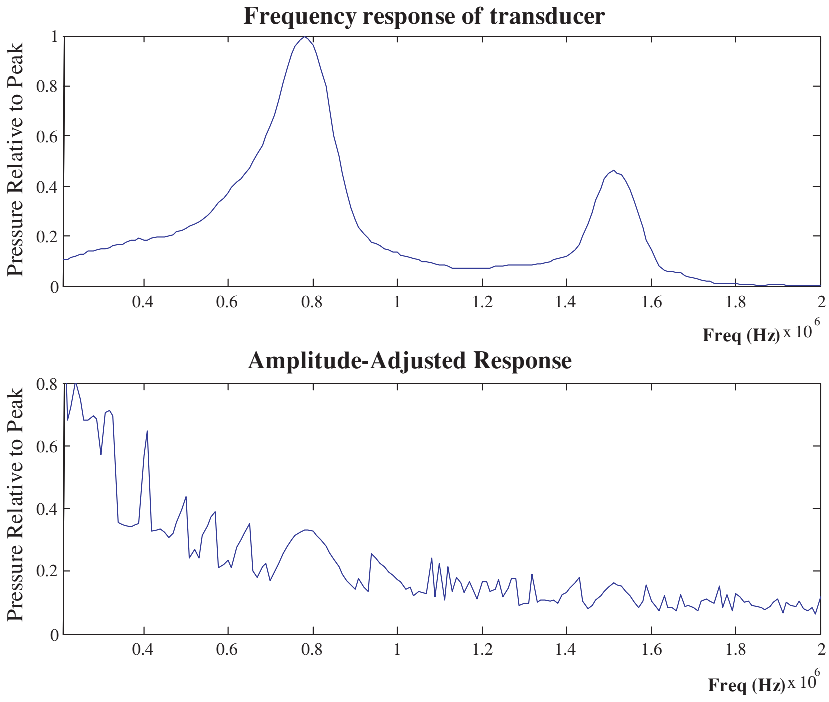

Figure 4. Send–receive frequency response of the transducer (above) before and (below) after the input voltage is adjusted to produce a more even amplitude across the relevant spectrum.

the initial pulse. For the pulsed waveform, the time history between 210 μs and 310 μs was recorded, and for the chirp, the time history between 210 μs and 410 μs was recorded. A schematic diagram is provided in figure 3.

For the multi-cycle excitations, 77 μs bursts were followed by a 923 μs rest period. Eight averages were acquired for each frequency step between 0.2 MHz and 2 MHz, which were taken at 0.01 MHz intervals. For the *fixed potential* measurements, the same electrical input was used for each frequency step. For the *fixed acoustic output*, amplitude was adjusted based on a response curve obtained by reflection from a steel plate. This frequency plot is shown in figure 4.

Chirped signals were created containing instantaneous frequencies comparable to the multi-cycle excitation,

$$p(t) = p_0 \sin(\omega_0 t + \beta t^2), \tag{7}$$

where the constant β is determined by the frequency range and T_{burst}, the signal time length:

$$\beta = \frac{\omega_{\max} - \omega_0}{2T_{\text{burst}}}, \tag{8}$$

using the values $\omega_0 = 1.26 \times 10^6$ rad s^{-1} (0.191 MHz), $\omega_{\max} = 1.26 \times 10^7$ rad s^{-1} (1.91 MHz) and $T_{\text{burst}} = 77 \times 10^{-6}$ s, giving $\beta = 7.3 \times 10^{10}$ rad s^{-2}. Received chirp signals were then cross-correlated with a reference signal. This reference was the reflection recorded after reflection off of a steel plate placed in the focus, normal to the axis of propagation.

All waveform data were analysed using Matlab (MathWorks Inc., Natick, MA). The envelope of the pulsed wave was determined using a sliding window function that selected

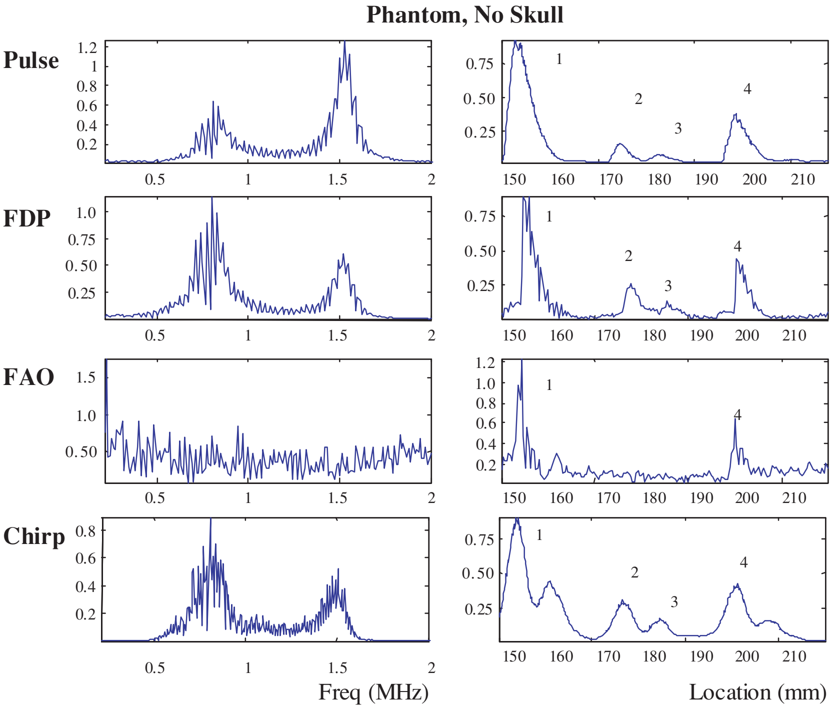

Figure 5. (Left) The spectrum and (right) the associated position determined from the signal received from a phantom using a pulse, a fixed driving potential (FDP), a fixed acoustic output (FAO) and a chirp. Values are normalized to signal maxima.

the mean amplitude over a 2.9 μs window. The chirped signal was cross-correlated with its reference signal to recover the peaks and the multi-cycle data were processed using a discrete approximation to equation (5). For all methods the time of flight was selected in a semi-automatic fashion, where an algorithm determined the peaks within user-defined regions on the plots.

4. Results

4.1. Baseline measurement

Measurements were first acquired using the phantom without a skull fragment. Transskull data were subsequently compared to these measurements. For each time reconstruction, the location, peak amplitude, noise level and full width at half maximum (FWHM) were determined. Location was taken to be equal to half the product of the time of flight and the sound speed. Four peak regions were manually identified by examination of the time histories (figure 5), and a reconstruction algorithm then automatically identified peak amplitudes and FWHM values in each of the four regions. Figures 5–8 show both the frequency and the time domain of the signals. The signal for the pulsed and chirped signals was measured in the time domain, with their corresponding frequency spectra calculated from a Fourier transform. Conversely, the multiple-cycle measurements were assembled in the frequency domain and the positions were determined from the inverse transform of the product on the right-hand side of equation (5). Using the pulsed waveform reconstruction as a reference, the positions

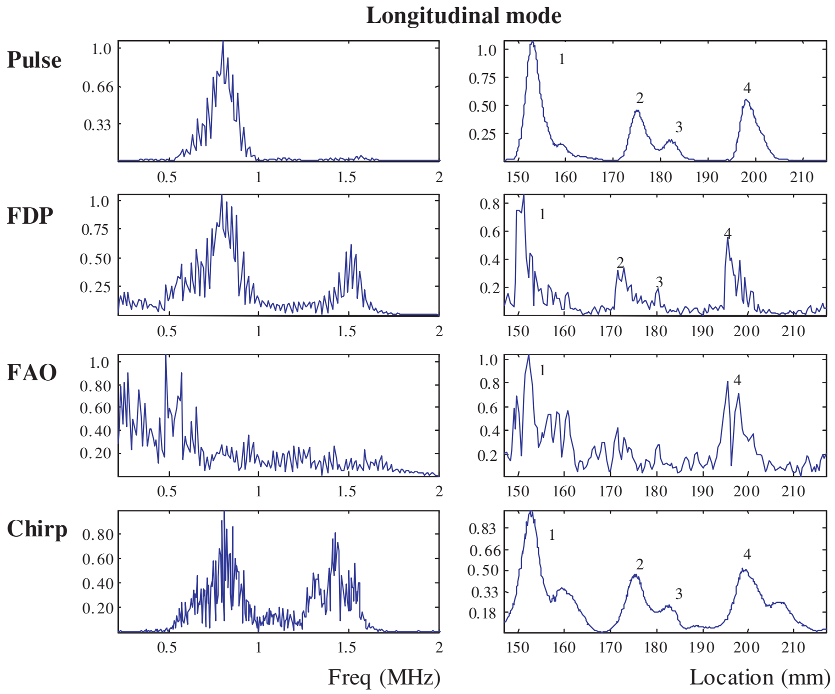

Figure 6. (Left) The spectrum and (right) the associated position determined from the signal received from the phantom in figure 5, but with a skull placed approximately perpendicular to the axis of propagation using a pulse, a fixed driving potential (FDP), a fixed acoustic output (FAO) and a chirp.

Table 1. Position, phantom without skull, mean and standard deviation are calculated from results of nine skull samples.

	Interface			
	d_1 (mm)	d_2 (mm)	d_3 (mm)	d_4 (mm)
Measured	150.0	170.0	180.0	200.0
Pulse	153.9 ± 0.5	175.8 ± 0.5	183.7 ± 0.5	199.2 ± 0.4
Fixed potential	155.1 ± 0.3	178.0 ± 0.5	185.8 ± 0.5	200.6 ± 0.5
Fixed acoustic output	154.7 ± 0.3			200.4 ± 0.3
Chirp	154.1 ± 0.6	176.9 ± 0.6	184.6 ± 0.7	202.6 ± 0.7

were determined to be at locations 153.9 ± 0.5 mm, 175.8 ± 0.5 mm, 183.7 ± 0.5 mm and 199.2 ± 0.4 mm. A comparison of position measurements using each measurement modality is provided in table 1.

Signals shown in figure 5 revealed peaks corresponding to each of the four scattering surfaces using the pulsed, *fixed potential* multi-cycle and chirped signals. The *fixed acoustic output* method detected the phantom interfaces with sharper peaks than the other methods. This may be represented quantitatively as the FWHM of the signal peaks. These values are summarized in table 2, showing reduced peaks for the two multi-cycle methods. However, this increased localization was achieved at the expense of increased noise, resulting in the

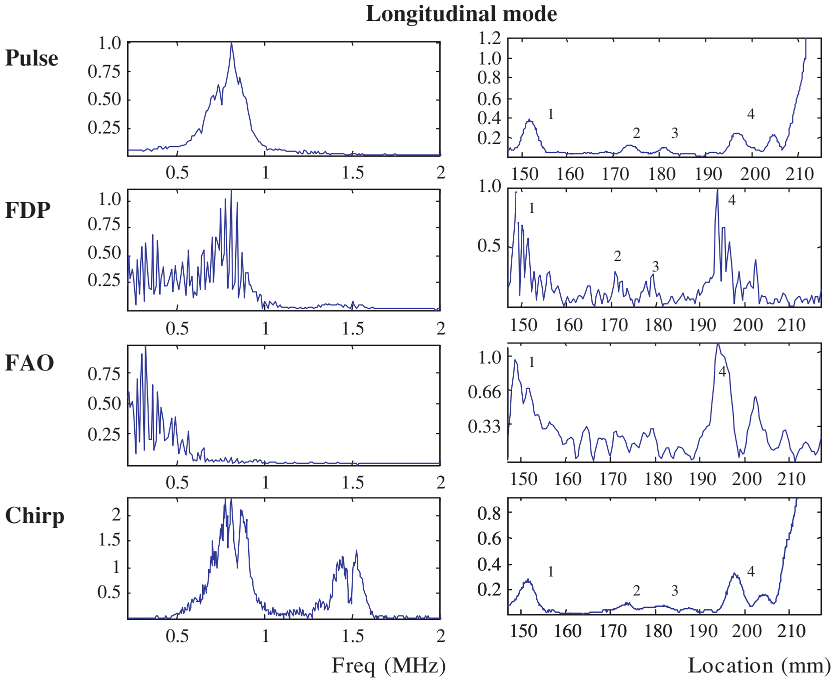

Figure 7. (Left) The spectrum and (right) the associated position determined from the signal received from the phantom in figure 5. Perpendicular alignment similar to figure 6 is used, but in this case the pulse and chirp both contain a strong peak near 210 mm due to scattering artefacts caused by the skull bone.

Table 2. FWHM, phantom without skull ($N = 9$).

	Interface			
	d_1 (mm)	d_2 (mm)	d_3 (mm)	d_4 (mm)
Pulse	4.3 ± 0.5	3.7 ± 0.5	4.9 ± 0.5	4.4 ± 0.5
Fixed potential	3.1 ± 0.3	3.3 ± 0.3	4.1 ± 0.3	2.5 ± 0.3
Fixed acoustic output	1.6 ± 0.6			2.0 ± 0.3
Chirp	5.3 ± 0.5	4.8 ± 0.5	5.0 ± 0.5	5.7 ± 0.7

inability to detect the two embedded wires in the case of the *fixed acoustic output* approach. Examination of the chirp signal revealed artefacts, which appeared as secondary peaks after the primary reflection, adding ambiguity as to the localization of the objects.

4.2. Longitudinal and shear modes

With the skull in place, localized signal peaks were observed with each of the four measurement methods for both the longitudinal and shear modes in the skull. Nine locations were selected from skull fragments from three different formaldehyde-preserved skulls. Measurements through each of these locations were used to determine the overall means and standard deviations for the pulse, chirp and multi-cycle methods in longitudinal and shear modes.

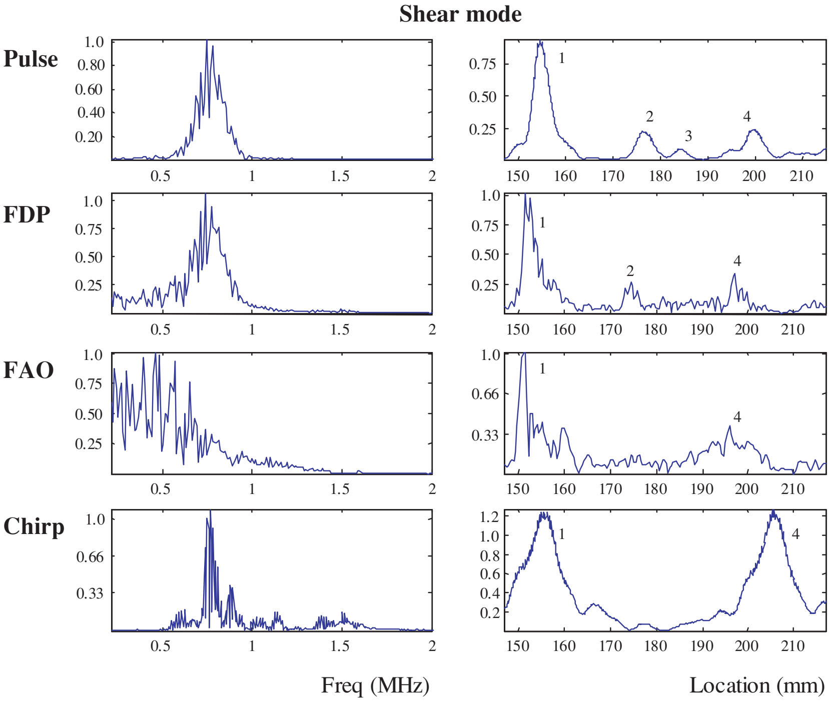

Figure 8. (Left) The spectrum and (right) the associated position determined from the signal received from the phantom in figure 6, but with a skull placed at angles greater than 30° relative to the axis of propagation using a pulse, a fixed driving potential (FDP), a fixed acoustic output (FAO) and a chirp.

These values allowed for comparison of the different output signals as well as an evaluation of the use of shear mode versus longitudinal modes. An example of a transskull reconstruction at normal skull incidence is shown in figure 6. The longitudinal mode was also found to be prone to artefacts caused by mixing of the signal with reflections from the skull surface, often causing an inability to measure the second surface of the phantom or adding an artificial peak in the data. A similar longitudinal measurement with a different skull sample is shown in figure 7, providing an example of pulsed and chirped signals with a strong artefact due to bone reflection, which do not appear in the multi-cycle method due to its time windowing. These artefacts were most prevalent in the case of the chirped signal, due to the extension in time of the reflections from bone layers into the time window of the ROI. A higher number of successful reconstructions were observed in cases of high angular incidences (figure 8), in the sense of correctly identifying the location of the objects and a reduced occurrence of artefacts from bone reflections.

A summary of the measurements performed at normal incidence is presented in figure 9. This figure shows the mean location of the measurement peaks with (circles) and without (squares) the skull. The transskull measurements have been linearly scaled so that the amplitudes of the first peak both with and without the skull are equal. Horizontal and vertical error bars represent the standard deviation in the position and the normalized amplitudes, respectively. Comparison of the locations with and without the skull indicates an expected systematic shift of the peaks as a result of the faster sound speed in the skull. The same

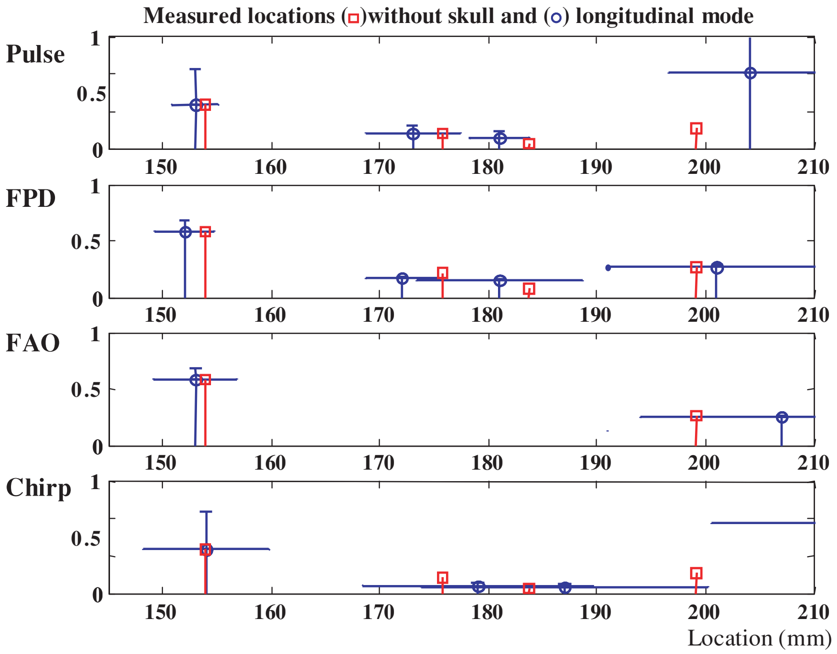

Figure 9. Mean measured locations of the four highest signal peaks with the skull perpendicular to the axis of propagation (circle) and without (square) the skull bone.

Table 3. FWHM, differences (mm) between measurements using shear and longitudinal modes. Negative values indicate that the longitudinal approach was superior ($N = 9$).

	Interface			
	d_1 (mm)	d_2 (mm)	d_3 (mm)	d_4 (mm)
Improvement in position, SW versus longitudinal				
Pulsed	0.72	2.6	0.4	4.7
Fixed potential	0	3.6	−0.64	−0.33
Fixed acoustic output	0.72			7
Chirp	−2	2	−6	10
Improvement in FWHM, SW versus longitudinal				
Pulse	−2.7	−2.5	−1.4	−2.7
Fixed potential	−0.73	−2.1	−1.2	0.26
Fixed acoustic output	−0.44			−2.6
Chirp	−1.1	−2.9	0.49	−1.7

plot with the shear mode of transskull propagation is given in figure 10. Differences between figures 9 and 10 indicate better accuracy in determination of the location of the scatterers when using the shear mode. However, the longitudinal mode was superior in nearly all cases for localization (FWHM) of the beam. Table 3 summarizes these differences. The origin of these broadened FWHMs can be seen in frequency plots of figures 7 and 8, which indicate a reduction in the bandwidth in the case of shear mode propagation due to increased attenuation at frequencies above 1 MHz relative to the longitudinal counterpart.

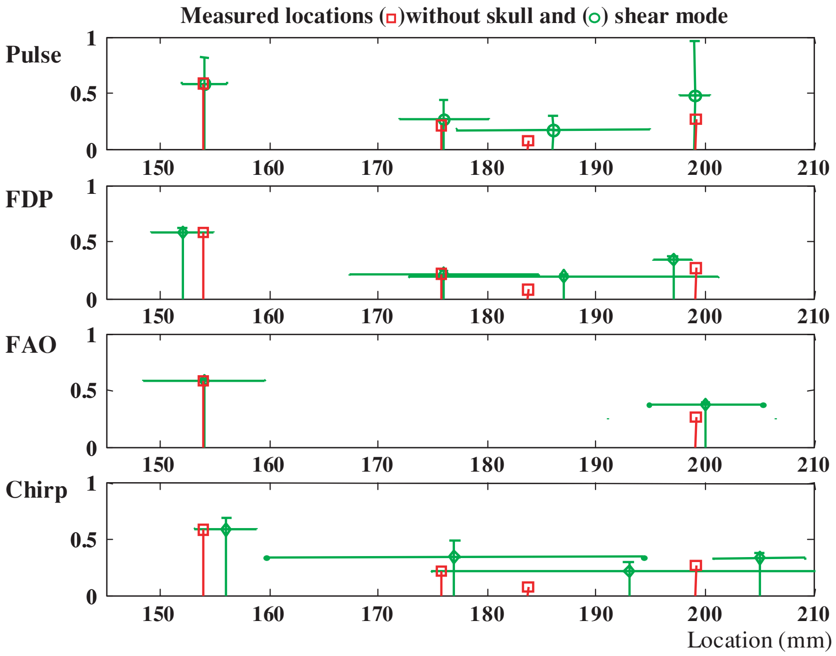

Figure 10. Mean measured locations of the four highest signal peaks with the skull oriented greater than 30° relative to the axis of propagation (circle) and without (square) the skull bone.

5. Discussion

This paper describes preliminary experiments in transcranial measurement using a multi-cycle approach. The purposes of the study were to determine the ability of the multi-cycle schemes to detect scattering sources within a predetermined ROI, to compare this approach to pulsed and chirped waveforms and to assess its ability to function through human skull bone. Compared to a broadband pulse, the multi-cycle techniques were found to produce more localized peaks at scattering interfaces of a tissue phantom consisting of the phantom's front and rear surfaces, and two 0.5 mm embedded nylon wires.

Position measurements summarized in table 1 indicate that the first three, but not the fourth reflection, were overestimated, even without the presence of a skull. It is believed this is due, at least in part, to the choice of the local signal maxima as the measurement point for time of flight. This approach potentially introduced a systematic error in the position measurements. If this is the case, then it is the time-of-flight measurement of the fourth reflection that may actually be distorted. This could be caused by the cumulative propagation of error in the time of flight, due to initial error in the value used for the phantom's sound speed.

Based on the present work, it is expected that the full frequency range transmitted through bone with the multi-cycle approach could be sampled in a reasonable time. For example, a frequency window extending from 0.2 MHz to 1.8 MHz over a 50 mm ROI would require 107 frequency steps. Acquired as a 5% duty cycle of a 1 ms pulse (50 μs burst length), a full acquisition would take 100 ms times the number of desired averages.

When a skull fragment was added between the transducer and the phantom, less distortion in the position of the scattering surfaces resulted when using a shear mode of ultrasound propagation through the bone. However, in this mode, a broadened FWHM resulted and

Table 4. FWHM (mm) for longitudinal propagation ($N = 9$).

	Interface							
	d_1 (mm)		d_2 (mm)		d_3 (mm)		d_4 (mm)	
Pulse	4.5 ± 1.4	$p = 0.03$	5.3 ± 1.5	$p = 0.23$	5.2 ± 1.9	$p = 0.06$	5.5 ± 3.4	$p = 0.52$
Fixedpotential	3.1 ± 1.1		4.2 ± 2.1		3.5 ± 1.7		4.4 ± 3.7	
Fixed acoustic output	6.8 ± 4.6						7.3 ± 3.8	
Chirp	7.8 ± 5.7		7.4 ± 4.5		9.4 ± 4.3		11. ± 8.0	

Table 5. FWHM (mm) for shear propagation ($N = 9$).

	Interface							
	d_1 (mm)		d_2 (mm)		d_3 (mm)		d_4 (mm)	
Pulse	7.2 ± 6.7	$p = 0.05$	7.8 ± 7.0	$p = 0.61$	6.6 ± 2.4	$p = 0.06$	8.2 ± 3.7	$p = 0.02$
Fixed potential	3.9 ± 2.6		6.4 ± 3.7		4.6 ± 1.8		4.2 ± 2.6	
Fixed acoustic output	7.3 ± 5.9						9.9 ± 4.3	
Chirp	8.9 ± 4.2		10 ± 9.8		8.9 ± 3.8		13 ± 6.9	

the advantages of the multi-cycle technique were seen in the ‘soft tissue’ case, although, as indicated in tables 4 and 5, signals remained more localized when using the multi-cycle approach over a pulse. To assess statistical significance between the pulse and multi-cycle localization values, double-sided p-values were calculated. In the longitudinal case, two of these values were found to be statistically significant (d_1, t-value 2.4, p-value 0.03) or nearly significant (d_3, t-value 2.0, p-value 0.06). In the shear mode, two values were found to be statistically significant (d_1, t-value 2.1, p-value 0.05; d_4, t-value 2.7, p-value 0.02) and one nearly significant (d_3, t-value 2.0, p-value 0.06). Further, this approach did not experience the severe distortion due to bone reflections that was prevalent when using the chirped signal.

A clue to the cause of the distortion present with the chirp is presented in the spectral plots in figures 6–8. Examination of these plots reveals that a higher portion of the signal is present in the spectrum above 1 MHz, compared to all other methods. Since the skull is a strong attenuator at these frequencies, it is probable that these higher frequencies are, in fact, due to unavoidable mixing of the desired signal with reflections from the skull surface. Similar reflections are naturally removed by the time windowing used with the other three methods.

The *fixed acoustic output* measurements were observed to have the sharpest and most accurate signal peak, suggesting that a trade-off is necessary between the added bandwidth and the noise introduced by the approach with the present transducer. To perform these measurements, the amplitudes near resonance had to be performed at lower amplitude than the fixed potential case because of the limits on the linear behaviour of the transducer off resonance. That is, upper limits on the amplitude were required due to nonlinear output caused by driving a hard restoring oscillator at off-resonant frequencies (Morse and Ingard 1968). Consequently, amplitudes were set just below the point where the nonlinear or ‘hard’ restoring nature of the transducer was apparent on the oscilloscope.

A clear drawback of using the transskull shear mode was a broadening of the signal peaks as compared to the longitudinal mode. The primary reason for this broadening is evident upon examination of the received spectrum, which showed increased attenuation at high frequencies relative to the longitudinal case. A simple solution to this attenuation would be to maintain the bandwidth of the present transducer while reducing the centre frequency. However, this clearly will result in an increased beamwidth, which would ultimately manifest itself in low radial image resolution in 2D imaging. Thus, future work will centre on combining the methods proposed in this paper with scattering techniques that recover radial resolution in the presence of lower frequencies.

Although the present work is limited to A-mode images, the approach is expected to generalize to higher dimensional imaging. Successful implementation in two or three dimensions could allow transcranial imaging with both a higher net input power and a higher axial resolution than existing methods. While the motivation for the study was enhanced ultrasound propagation through the human skull, the approach may also find additional applications in other situations where highly attenuating media are located between the source and the object to be detected.

Acknowledgment

This work was supported by US National Institutes of Health NIBIB grant no EB004353.

References

Aubry J F, Tanter M, Pernot M, Thomas J-L and Fink M A 2003 Experimental demonstration of noninvasive transskull adaptive focusing based on prior computed tomography scans *J. Acoust. Soc. Am.* **113** 84–93

Baikov S V, Babin L V, Molotilov A M, Neiman S I, Riman V V, Svet V D and Selyanin A I 2003a Physical and technical aspects of ultrasonic imaging of brain structures through thick skull bones: 2. Experimental studies *Acoust. Phys.* **49** 465–73

Baikov S V, Molotilov A M and Svet V D 2003b Physical and technical aspects of ultrasonic imaging of brain structures through thick skull bones: 1. Theoretical and model studies *Acoust. Phys.* **49** 276–84

Barrows H S, Kurze T, Leeds N E, Dyck P and McCormick R A A 1964 Echoencephalography—diagnostic use of ultrasound in suspected brain injury *Neurology* **14** 274

Becker G, Krone A, Koulis D, Lindner A, Hofmann E, Roggendorf W and Bogdahn U 1994 Reliability of transcranial color-coded real-time sonography in assessment of brain-tumors—correlation of ultrasound, computed-tomography and biopsy findings *Neuroradiology* **36** 585–90

Berg D and Becker G 2002 Perspectives of B-mode transcranial ultrasound *NeuroImage* **15** 463–73

Britt R H, Lyons B E, Enzmann D R, Saxer E L, Bigner S H and Bigner D D 1987 Correlation of neuropathologic findings, computerized tomographic and high-resolution ultrasound scans of canine avian-sarcoma virus-induced brain-tumors *J. Neurooncol.* **4** 243–68

Clement G T and Hynynen K 2002 A noninvasive method for focusing ultrasound through the human skull *Phys. Med. Biol.* **47** 1219–36

Clement G T, White P J and Hynynen K 2004 Enhanced ultrasound transmission through the human skull using shear mode conversion *J. Acoust. Soc. Am.* **115** 1356–64

Dines K A, Fry F J, Patrick J T and Gilmor R L 1981 Computerized ultrasound tomography of the human head—experimental results *Ultrason. Imaging* **3** 342–51

Erikson K R, Fry F J and Jones J P 1974 Ultrasound in medicine—review *IEEE Trans. Sonics Ultrason.* **21** 144–70

Fry W J 1968 Intracranial anatomy visualized *in vivo* by ultrasound *Invest. Radiol.* **3** 243–66

Fry F J and Barger J E 1978 Acoustic properties of the human skull *J. Acoust. Soc. Am.* **63** 1576–90

Grossman C C 1964 Clinical diagnostic application of ultrasound in brain disorders (sono-encephalography) *Dis. Nerv. Syst.* **25** 403

Harrer J U, Mayfrank L, Mull M and Klotzsch C 2003 Second harmonic imaging: a new ultrasound technique to assess human brain tumour perfusion *J. Neurol. Neurosurg. Psychiatry* **74** 333–8

Koivukangas J, Ylitalo J, Alasaarela E and Tauriainen A 1986 3-Dimensional ultrasound imaging of brain for neurosurgery *Ann. Clin. Res.* **18** 65–72

Madsen E L, Frank G R and Dong F 1998 Liquid of solid ultrasonically tissue-mimicking materials with very low scatter *Ultrasound Med. Biol.* **24** 535–42

Misaridis T X, Gammelmark K, Jorgensen C H, Lindberg N, Thomsen A H, Pedersen M H and Jensen J A 2000 Potential of coded excitation in medical ultrasound imaging *Ultrasonics* **38** 183–9

Misaridis T and Jensen J A 2005a Use of modulated excitation signals in medical ultrasound: Part I. Basic concepts and expected benefits *IEEE Trans. Ultrason. Ferroelectr. Freq. Control* **52** 177–91

Misaridis T and Jensen J A 2005b Use of modulated excitation signals in medical ultrasound: Part II. Design and performance for medical imaging applications *IEEE Trans. Ultrason. Ferroelectr. Freq. Control* **52** 192–207

Montaldo G, Aubry J F, Tanter M and Fink M 2005 Spatio-temporal coding in complex media for optimum beamforming: the iterative time-reversal approach *IEEE Trans. Ultrason. Ferroelectr. Freq. Control* **52** 220–30

Morse P M and Ingard K U 1968 *Theoretical Acoustics* (Princeton, NJ: Princeton University Press)

O'Donnell M and Flax S W 1988 Phase aberration measurements in medical ultrasound: human studies *Ultrason. Imaging* **10** 1–11

Pedersen M H, Misaridis T X and Jensen J A 2003 Clinical evaluation of chirp-coded excitation in medical ultrasound *Ultrasound Med. Biol.* **29** 895–905

Seidel G, Algermissen C, Christoph A, Claassen L, Vidal-Langwasser M and Katzer T 2000 Harmonic imaging of the human brain—visualization of brain perfusion with ultrasound *Stroke* **31** 151–4

Shen J and Ebbini E S 1996 A new coded-excitation ultrasound imaging system: Part I. Basic principles *IEEE Trans. Ultrason. Ferroelectr. Freq. Control* **43** 131–40

Shigemori M, Moriyama T, Harada K, Kikuchi N, Tokutomi T and Kuramoto S 1990 Intracranial hemodynamics in diffuse and focal brain injuries—evaluation with transcranial Doppler (TCD) ultrasound *Acta Neurochir.* **107** 5–10

Smith S W, Chu K, Idriss S F, Ivancevich N M, Light E D and Wolf P D 2004 Feasibility study: real-time 3D ultrasound imaging of the brain *Ultrasound Med. Biol.* **30** 1365–71

Smith S W, Phillips D J, von Ramm O T and Thurstone F L 1979 *Some Advances in Acoustic Imaging Through the Skull* (Washington, DC: National Bureau of Standards) pp 209–18

Smith S W, Ramm O T V, Kisslo J A and Thurstone F L 1978 Real-time ultrasound tomography of adult brain *Stroke* **9** 117–22

Wall P D, Tucker D, Fry F J and Mosberg W H 1953 The use of high intensity ultrasound in experimental neurology *J. Acoust. Soc. Am.* **25** 281–5

White P J 2005 Modalities for optimization of ultrasound transmission through the human skull *Acoustics Doctoral Dissertation* Penn State University

Wiesmann M and Seidel G 2000 Ultrasound perfusion imaging of the human brain *Stroke* **31** 2421–5